

ARTICLE OPEN



Possible star-of-David pattern charge density wave with additional modulation in the kagome superconductor CsV₃Sb₅

J. Luo^{1,7}✉, Z. Zhao^{1,2,7}, Y. Z. Zhou^{1,2}, J. Yang¹, A. F. Fang³, H. T. Yang^{1,2,4}✉, H. J. Gao^{1,2,4,5}, R. Zhou^{1,4}✉ and Guo-qing Zheng^{1,6}

AV₃Sb₅ (A = K, Rb, Cs) is a novel kagome superconductor coexisting with the charge density wave (CDW) order. Identifying the structure of the CDW order is crucial for understanding the exotic normal state and superconductivity in this system. Here, we report ⁵¹V nuclear magnetic resonance (NMR) and ^{121/123}Sb nuclear quadrupole resonance (NQR) studies on kagome-metal CsV₃Sb₅. Below the CDW transition temperature $T_{\text{CDW}} \sim 98$ K, an abrupt change of spectra was observed, indicating that the transition is of the first order. By further analyzing the spectra, we find that the CDW order is commensurate. And most remarkably, the obtained experimental results suggest that the charge modulation of the CDW order is of star-of-David pattern and accompanied by an additional charge modulation in bulk below $T^* \sim 40$ K. Our results revealing the unconventional CDW order provide new insights into AV₃Sb₅.

npj Quantum Materials (2022)7:30; <https://doi.org/10.1038/s41535-022-00437-7>

INTRODUCTION

Compounds with kagome or honeycomb lattices provide a rich material base for exploring exotic physical phenomena, including topological electronic states¹, highly frustrated magnetisms^{2–4}, and quantum spin liquids^{5–9}. They are perfect platforms to study the relation between topology, frustration, and electron correlation. However, materials with geometrically frustrated lattices showing superconductivity are still very limited.

Recently, a new transition metal family AV₃Sb₅ (A = K, Rb, Cs) with perfect vanadium kagome-net was found¹⁰. Angle-resolved photoemission spectroscopy (ARPES), Shubnikov de Haas (SdH) oscillations and density functional theory (DFT) studies categorize AV₃Sb₅ into a Z₂ topological class with non-trivial topological bands^{11,12}. Furthermore, the AV₃Sb₅ system was found to be superconducting with T_c range from 0.9 K to 3 K^{12,13}. Above T_c , another phase transition exists at 80 K ~ 100 K revealed by magnetic susceptibility and resistivity measurements^{10,13}. Scanning tunneling microscopy (STM), optical spectroscopy and ARPES experiments infer that the phase transition around $T = 80$ K ~ 100 K is a CDW transition^{14–21}. In the CDW state, hard X-ray scattering and STM measurements observe a $2a_0 \times 2a_0 \times 2c_0$ superlattice^{14,22–26}. A star-of-David distortion, found in the known CDW of 1T-TaS₂²⁷, was assumed in the kagome plane^{14,22,28}. As the cleavage surface is A or Sb plane, STM measurements can not directly detect the charge modulation in the vanadium kagome plane. Based on the DFT calculations, an inverse deformation to the star-of-David structure, Tri-hexagonal pattern, was suggested to be the distorted structure^{19,29,30}. However, this has not been clarified by any microscopic probe in the kagome plane yet. Moreover, a $4a_0$ charge modulation was suggested to emerge inside the CDW state below $T \sim 60$ K^{24,28}. The additional charge modulation along the c -axis was also reported by X-ray scattering studies³⁰, while not confirmed by other STM and X-ray scattering studies^{22,23}.

Experiments under pressure further elaborated the importance of the CDW order. Transport measurements show that applying pressure can suppress the CDW order and enhance T_c by almost three times in AV₃Sb₅^{31–34}, making the pressure-temperature phase diagram resemble many unconventional superconductors^{35,36}. This behavior suggests a close relationship between CDW and superconductivity. The emergence of the pairing density wave in the superconducting state, which might be due to the influence of the CDW order, seems further support this view²⁴. In the current stage, the structure of the CDW order in AV₃Sb₅ is still indistinct and identifying it is very important for understanding the origin of the CDW order and its relation to the superconductivity.

In this work, we have performed ⁵¹V nuclear magnetic resonance (NMR) and ^{121/123}Sb nuclear quadrupole resonance (NQR) measurements on CsV₃Sb₅. By studying the spectra at low temperatures, we demonstrate that the CDW order is commensurate and our result is consistent with the star-of-David type structural distortion. Below $T^* \sim 40$ K, a further line splitting is observed in ⁵¹V-NMR spectra, while a line broadening was observed in ¹²¹Sb-NQR spectra. This behavior implies the appearance of an additional charge modulation and further demonstrates the unconventional nature of the CDW order.

RESULTS AND DISCUSSIONS

Charge density wave order: ⁵¹V-NMR results

In the crystal structure of CsV₃Sb₅ shown in Fig. 1(a), three V atoms constitute one triangle which is corner-shared to other V triangles, forming a perfect V-kagome lattice. In the unit cell, all V sites are equivalent. A magnetic field of $B_0 = 11.997$ T along the c -axis is applied for ⁵¹V-NMR measurements. The total Hamiltonian under

¹Institute of Physics, Chinese Academy of Sciences, and Beijing National Laboratory for Condensed Matter Physics, Beijing 100190, China. ²School of Physical Sciences, University of Chinese Academy of Sciences, Beijing 100190, China. ³Department of Physics, Beijing Normal University, Beijing 100875, China. ⁴Songshan Lake Materials Laboratory, Dongguan, Guangdong 523808, China. ⁵CAS Center for Excellence in Topological Quantum Computation, University of Chinese Academy of Sciences, Beijing 100190, China. ⁶Department of Physics, Okayama University, Okayama 700-8530, Japan. ⁷These authors contributed equally: J. Luo, Z. Zhao. ✉email: junluo@iphy.ac.cn; htyang@iphy.ac.cn; rzhou@iphy.ac.cn

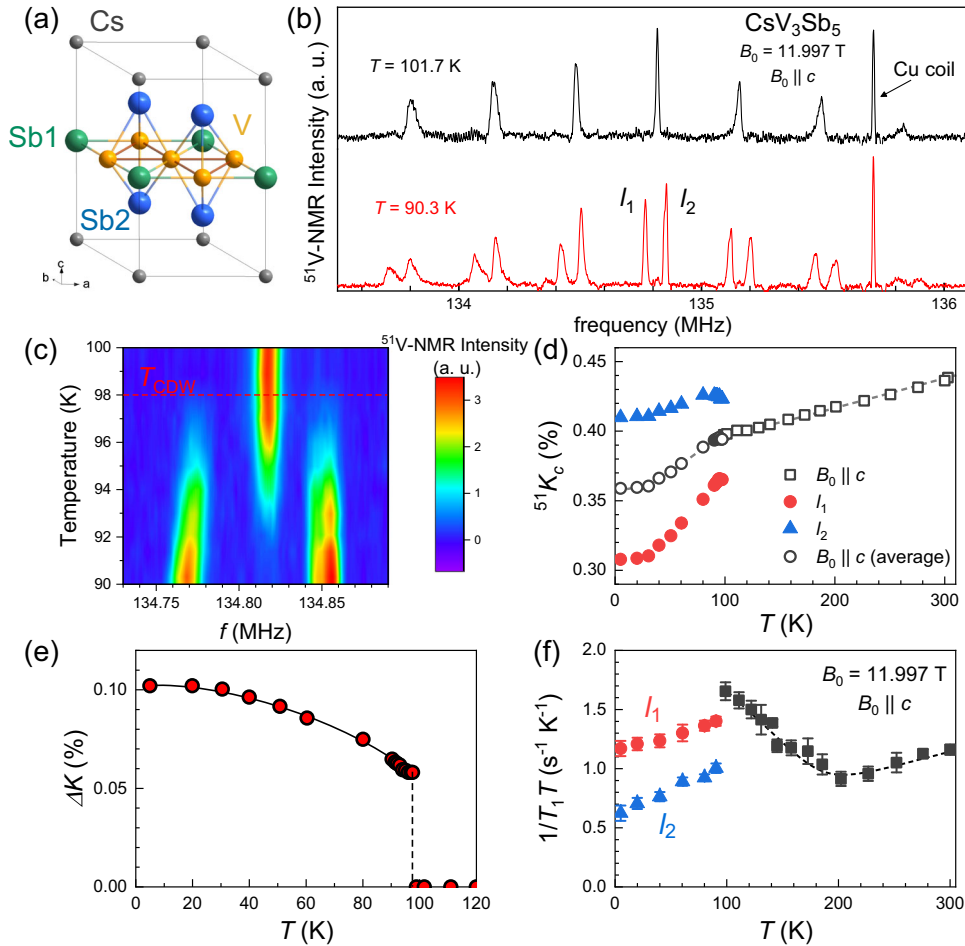


Fig. 1 ^{51}V -NMR evidence for the CDW order. **a** The crystal structure of CsV_3Sb_5 at room temperature. **b** Temperature dependence of the ^{51}V -NMR spectra above T_{CDW} (black color) and below T_{CDW} (red color) with the external magnetic field applied along the c -axis. The low- and high-frequency central peaks of 90.3 K were assigned as I_1 and I_2 , respectively. The sharp peak around 135.7 MHz is from the Cu coil. **c** Contour plot of the ^{51}V central lines around T_{CDW} , there are three peaks between 98 K and 92 K. **d** Temperature dependence of the Knight shift K_c for ^{51}V central line. The average K_c of the two peaks is plotted by black circles. **e** Temperature dependence of the Knight shift difference ΔK between the two split peaks. **f** Temperature-dependent $1/T_1T$ for ^{51}V measured at the central lines. Below T_{CDW} , $1/T_1T$ and K_c of I_1 and I_2 are plotted by red dots and blue triangles, respectively. The dash lines are the guides to the eyes. The error bar of $1/T_1T$ is the s. d. in fitting the recovery curve.

magnetic field is³⁷:

$$\mathcal{H} = \mathcal{H}_0 + \mathcal{H}_Q = -\gamma\hbar\mathbf{l} \cdot \mathbf{B}_0(1 + K) + \frac{e^2qQ}{4I(2I-1)} \left[(3I_z^2 - I^2) + \frac{1}{2}\eta(I_+^2 + I_-^2) \right] \quad (1)$$

where K is the Knight shift, $eq = V_{\text{ZZ}} = \frac{\partial V^2}{\partial z^2}$ is the electric field gradient (EFG) along the principal axis, and V is the electric potential, Q is the nuclear quadrupole moment, and $\eta = |V_{\text{XX}} - V_{\text{YY}}|/|V_{\text{ZZ}}|$ is the asymmetry parameter of EFG. The nuclear quadrupole resonance frequency ν_Q is defined as $\frac{3e^2qQ}{2I(2I-1)\hbar}$. γ is the nuclear gyromagnetic ratio, which is 11.193 MHz/T for the ^{51}V nucleus. Since the nuclear spin I of ^{51}V is $7/2$, there should appear seven transition lines. Indeed, the ^{51}V -NMR spectrum at 101.7 K (above T_{CDW}) shown in Fig. 1(b) consists of one central peak and six satellite peaks. With decreasing temperature down to 90.3 K, we find that all NMR lines split into two lines with area ratio around 1:1 as illustrated in the bottom of Fig. 1(b). No spectral weight is lost during the transition. We also note that the splitting of the first low-frequency satellite, $\delta f_{\text{satellite}} = 0.0818$ MHz, is different from the splitting of the central peak, $\delta f_{\text{center}} = 0.0842$ MHz, indicating that both magnetic and quadrupole shifts contribute to the observed line splitting. This behavior is the same

with the CDW order in $\text{YBa}_2\text{Cu}_3\text{O}_y$ and $\text{Bi}_2\text{Sr}_{2-x}\text{La}_x\text{CuO}_{6+\delta}$ ^{38,39}, suggesting that a charge modulation occurs at low temperatures. For the one dimensional (1D) incommensurate CDW order, the NMR spectrum should have two peaks of equal intensities, and most importantly, a continuum between the two peaks⁴⁰. For the 2D or 3D cases, if the amplitude of the charge modulation along one direction is much stronger than the others, the NMR spectrum should be similar to the 1D incommensurate CDW order⁴⁰. Otherwise, the spectrum should only have one symmetric peak⁴⁰. These features for the incommensurate CDW are not observed in ^{51}V -NMR spectra, indicating that the observed CDW order is not incommensurate. On the other hand, the commensurate CDW results in discrete peaks⁴¹, which is consistent with our observation, proving that the CDW order is commensurate.

To further investigate the CDW evolution, we make a contour plot of the central lines from $T = 100$ to 90 K, as shown in Fig. 1(c) (the raw data is shown in Supplementary Fig. 2). Three lines are seen between $T = 98$ K and 93 K, implying the coexistence of the CDW and a charge-uniform phase. With decreasing temperature, the NMR intensity gradually shifts from the line of the charge-uniform state to the two split lines related to the CDW state. These are the typical features of the first-order transition. We fit the ^{51}V -NMR spectra with the Lorentz function to get the resonance

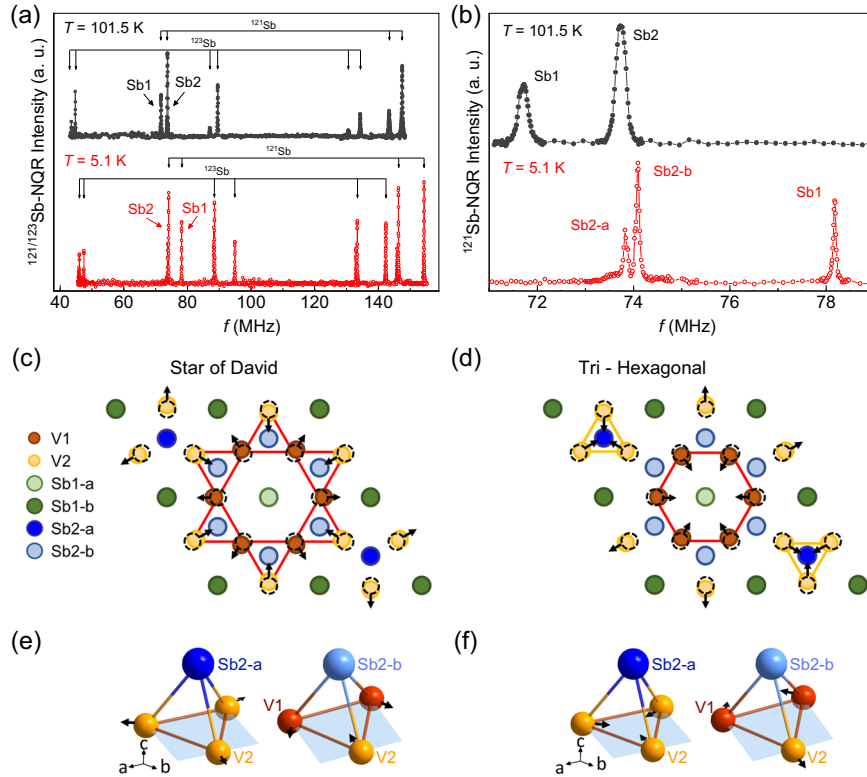


Fig. 2 $^{121/123}\text{Sb}$ -NQR spectra and illustration of possible CDW patterns. **a** The NQR spectra of $^{121/123}\text{Sb}$ at 101.5 K (above T_{CDW}) and 5.1 K (below T_{CDW}). There are five pairs of resonance peaks in the spectrum above T_{CDW} , marked by five pairs of arrows. Each pair of resonance peaks comes from two types of Sb sites in the crystal structure, namely, Sb1 and Sb2. **b** Close-up of the spectrum between 71 MHz and 79 MHz, corresponding to $\pm 1/2 \leftrightarrow \pm 3/2$ transitions of ^{121}Sb . Below the CDW phase transition, one resonance peak from Sb2 splits into two peaks marked as Sb2-a and Sb2-b, and the peak from Sb1 shifts to high frequency. The black dashed open circles represent the V site in the pristine crystal structure. The dark yellow and shallow yellow solid circles represent two types of V sites. The olive and shallow olive solid circles represent two types of Sb1 sites. The blue and shallow blue solid circles represent two types of Sb2 sites. **e**, **f** show the local structure around the Sb2 site in star-of-David and Tri-hexagonal patterns, respectively. The black arrows indicate the lattice distortion direction.

frequency f of central peaks. After subtracting the second-order perturbation from the quadrupole interaction (see Supplementary Note 3 for additional analysis), we obtain the temperature-dependent Knight shift K_c plotted in Fig. 1(d). The difference of the Knight shift between l_1 and l_2 is contributed from the spatial distribution of charge density in the CDW phase. ΔK is defined as the Knight shift difference of two split central peaks, and the results are summarized in Fig. 1(e). ΔK abruptly increases to non-zero at 98 K, which is consistent with the temperature dependence of the quadrupole frequency difference $\Delta\nu_Q$ (see Supplementary Fig. 4), again suggesting that the CDW transition is of the first order.

We further measure the temperature dependence of ^{51}V -NMR spin-lattice relaxation rate divided by T , $1/T_1T$, as shown in Fig. 1(f). The $1/T_1T$ decreases with decreasing T down to around 200 K but starts to increase towards T_{CDW} . Since Knight shift decreases with decreasing temperatures, the decrease of $1/T_1T$ at high temperatures might be due to the band effect as Co or Ni-doped BaFe_2As_2 systems^{42,43}. At low temperatures, the increase of $1/T_1T$ down to T_{CDW} can be due to either CDW or spin fluctuations. In view that the CDW transition is of the first order, the contribution from spin fluctuations should not be neglected⁴⁴. Below T_{CDW} , $1/T_1T$ is measured at both l_1 and l_2 lines, and both are found to decrease with decreasing temperature due to the gap opening in the CDW state. In the end, we note that the averaged Knight shift of two split lines is smaller than the extrapolation from high temperature K_c , suggesting a partial gap opening at the Fermi surface in the CDW state.

The structure of CDW order: $^{121/123}\text{Sb}$ -NQR results

Next, we use $^{121/123}\text{Sb}$ -NQR to obtain more information about the structure of the CDW order. There are two types of Sb sites in CsV_3Sb_5 . Namely, Sb1 is located in the center of the vanadium hexagon, and Sb2 is located above the vanadium triangle, as shown in Fig. 1(a). Sb has two type of isotopes, ^{121}Sb ($I = 5/2$) and ^{123}Sb ($I = 7/2$). For ^{121}Sb nucleus, the NQR spectrum should have two resonance peaks corresponding to $\pm 1/2 \leftrightarrow \pm 3/2$ and $\pm 3/2 \leftrightarrow \pm 5/2$ transitions. For ^{123}Sb nucleus, the NQR spectrum should have three resonance peaks corresponding to $\pm 1/2 \leftrightarrow \pm 3/2$, $\pm 3/2 \leftrightarrow \pm 5/2$ and $\pm 5/2 \leftrightarrow \pm 7/2$ transitions. So a total of ten lines should be observed in $^{121/123}\text{Sb}$ -NQR spectrum for CsV_3Sb_5 , which is indeed seen at $T > T_{\text{CDW}}$ in the normal state (see Fig. 2(a)). Considering that the atomic ratio between Sb1 and Sb2 is 1:4, we assign the lower and higher frequency line in each pair corresponding to Sb1 and Sb2, as indicated in the figure. Figure 2(b) shows the blow-up to compare the $^{121/123}\text{Sb}$ -NQR spectrum above and below T_{CDW} . With decreasing temperature, an abrupt change of the Sb-NQR spectrum was seen in the CDW state (see Supplementary Fig. 5). Unlike a simple splitting observed in the ^{51}V -NMR spectrum, the two Sb lines evolve into three in the the CDW state. We will show below how to assign these lines, and that the observed change of the Sb-NQR spectrum can be attributed to the star-of-David pattern in the CDW state.

Considering the atomic ratio between Sb1 and Sb2, we can assign that the two peaks around 74 MHz are from the Sb2 site, and another peak is from the Sb1 site. The frequencies of all lines are related to ν_Q and the asymmetry parameter η . The deduced ν_Q

and η as shown in Table 1 (the detailed calculation is presented in Supplementary Note 6). As the change of lattice parameter is $<1\%$ in the CDW state¹⁰, the main contribution to the EFG change should be from the unclosed $5p$ shell of Sb, similar to the case of the O site in the CuO_2 plane of the cuprate high- T_c superconductors⁴⁵. For the Sb1 site, the increase in ν_Q as large as 9% indicates a strong band renormalization at Sb1- p orbitals in the CDW state. Meanwhile, the absence of a change of η suggests that the renormalization should occur at the orbital along the principal axis of EFG, which is along the c -axis (see Supplementary Note 7). Therefore, our results suggest a strong band renormalization at Sb1- p_z orbital in the CDW state, which is consistent with ARPES results²¹. In contrast to the Sb1 site, ν_Q of the Sb2 site changes $<1\%$, suggesting that the band renormalization of the Sb2- p_z orbital is small. However, η increases to ~ 0.1 in the CDW state, suggesting a population disparity between Sb2- $5p_x$ and $5p_y$ orbitals, like the change of the As- $4p$ orbitals inside the nematic state in iron-based high- T_c superconductors^{46,47}. The population disparity between Sb2- $5p_x$ and $5p_y$ orbitals has not been captured by ARPES measurements so far, probably due to the limited energy resolution of the probe.

Along with the CDW transition, the star-of-David and Tri-hexagonal types of order as illustrated in Fig. 2(c) and (d), respectively, are proposed to be the possible structures^{14,29,48}. And based on these two proposed structures, we analyze our experimental results. These two types of order correspond to breathing-in and breathing-out phonon modes of the kagome lattice, respectively. The star-of-David type corresponds to the expansion of Sb1 centering V-hexagon and Sb2 centering V-triangle, and vice versa for the Tri-hexagon type. Both structures form a $2a_0 \times 2a_0$ superlattice. Previous STM and X-ray scattering experiments found that the charge modulation exhibits a π -phase shift along the c -axis, suggesting a three-dimensional $2a_0 \times 2a_0 \times$

$2c_0$ charge density wave ordering^{22,23}. For such ordering, the structural distortion pattern within different layers is the same. Moreover, considering that V and Sb1 sit in the V kagome plane and the Sb2 site is close to the plane, the main contribution to the EFG change should be from the in-plane structural distortion. In the analysis below, we only consider the structural distortion in the plane. In both star-of-David and Tri-hexagonal structures, two V sites exist with the atomic ratio of V1:V2 site = 1:1, which explains why ^{51}V -NMR central peak splits into two peaks with the area ratio of 1:1. The other feature for the proposed structures is that the Sb2 site should become two distinct sites, namely Sb2-a and Sb2-b as illustrated in Fig. 2(e) and (f). The atomic ratio of Sb2-a/Sb2-b should be 1:3. In our study, we find that the Sb2 peak indeed splits into two peaks with the ratio Sb2-a/Sb2-b around 1:3, which is consistent with both star-of-David and Tri-hexagonal patterns. We note that a structure with both star-of-David and Tri-hexagonal characters was reported³⁰. However, the coexistence of the two types of patterns will lead to four distinct Sb2 lines inside the CDW state, which is inconsistent with our observation. We note that more distinct V, Sb1 and Sb2 sites should emerge due to the influence of disorders or CDW domain boundaries. However, this is not observed in our NMR or NQR spectra, as shown in Figs. 1 and 2. Therefore, our observation suggests that disorders and CDW domain boundaries are rare in our sample. In principle, the Sb1 site can also become two distinct sites. As the six V atoms are very far from the Sb1 site, however, the difference between Sb1-a and Sb1-b site is very small, making the peak splitting unresolvable in the NQR spectrum.

Next, we distinguish between star-of-David and Tri-hexagonal patterns. For the star-of-David type structure, the average distance between Sb2-a and its nearest V atoms is longer than that between Sb2-b to its nearest V atoms. For the Tri-hexagonal structure, by contrast, the average distance between Sb2-a and its nearest V atoms is shorter than that between Sb2-b to its nearest V atoms. With the smaller distance between the V atom to the Sb atom, the influence to the local electron distribution of the Sb site will be more significant. By EFG calculation, we find that this will enhance the EFG of the Sb2 site (see Supplementary Note 7). Our result shows that the ν_Q of Sb2-a is smaller than that of Sb2-b (see Table 1 and Supplementary Fig. 5), suggesting the star-of-David structural distortion in the CDW state. Our observation is in contrast to the recent reports by combining DFT calculation with ultrafast pump-probe reflectivity experiments¹⁹, STM microscopy images²⁹, and quantum oscillation measurements³⁰, in which the Tri-hexagonal type structure distortion was suggested. In these studies, the electron correlation effect is not considered in the DFT calculation. Therefore, the neglected electron-electron interaction could be one possible reason for the contradiction between our and previous studies. However, we note that the displacement of

T	site	$\nu_Q(^{121}\text{Sb})$	$\nu_Q(^{123}\text{Sb})$	η
101.5 K	Sb1	71.716	43.520	0
	Sb2	73.728	44.763	0
5.1 K	Sb1-a /Sb1-b	78.179	47.456	0
	Sb2-a	73.039	44.370	0.0974
	Sb2-b	73.295	44.505	0.0991

The detailed calculation process of η can be found in Supplementary Note 6. The unit of ν_Q is MHz. η is a dimensionless parameter.

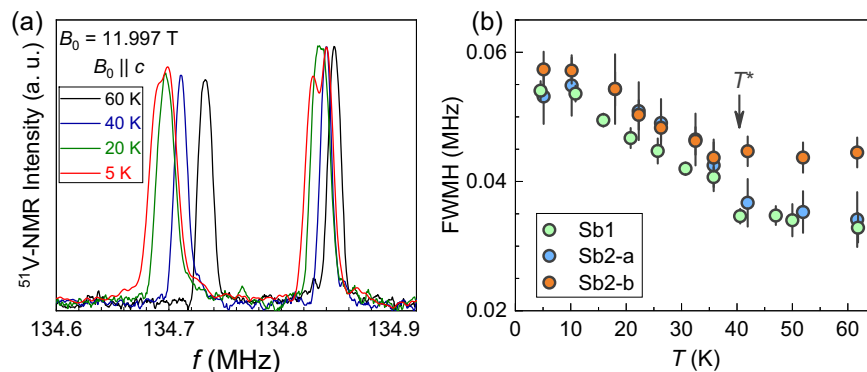


Fig. 3 Evidence for the additional charge modulation inside the CDW state. a Central peaks of ^{51}V -NMR spectra at various temperatures below $T = 60$ K. **b** Temperature-dependent full width of half maximum (FWHM) of all Sb sites. The FWHM of both sites start to increase below $T^* \sim 40$ K marked by the black arrow. The error bar is the s.d. in fitting spectra by the Lorentz function.

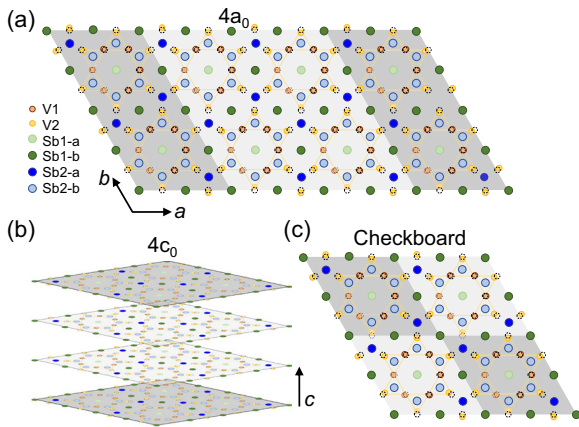


Fig. 4 Illustration of possible CDW patterns below T^* . $4a_0$, $4c_0$, and checkboard charge modulations compatible with the NMR spectra under the background of star-of-David type lattice distortion are shown in (a), (b), and (c), respectively. The gray level represents the charge density.

Sb atoms along c axis is not considered in our study based on the star-of-David and Tri-hexagonal patterns. It is also possible that the structure of the CDW pattern is much complex than the current proposed two structures. To further resolve this issue, NMR measurements on Sb sites are needed in the future.

Additional charge modulation inside the CDW state

Inside the CDW state, we further find another charge modulation at lower temperatures. As shown in Fig. 3(a), two central peaks of the V site start to broaden below $T^* \sim 40$ K, and further split into four at 5 K. Such further splitting is ten times smaller than the main splitting. So in a less clean sample, only a line broadening can be seen (see Supplementary Fig. 10), which also suggests that the splitting is not due to an impurity effect. The magnetic field is applied along the c -axis, which does not introduce any additional symmetry-breaking force. The possibility of magnetic phase transition can be excluded as there is no anomaly in the temperature dependence of $1/T_1T$ and the broadening is field-dependent (see Supplementary Fig. 11). Thus the change below T^* is mainly due to the Knight shift difference.

An orbital ordering could also cause a Knight shift splitting^{47,49}. Note, however, that the NMR line splitting inside the orbital-ordered state is due to the formation of twinned domains^{47,49}. In different domains, the applied magnetic field is along different axes, resulting in the line splitting. For a de-twinned sample, only a frequency shift was seen due to the orbital ordering⁵⁰. For NQR measurements, on the other hand, no external magnetic field was applied, so the spectra for different domains are the same, resulting in a move of the NQR spectrum below the ordering temperature as seen in $\text{LaFeAsO}_{1-x}\text{F}_x$ ⁵¹ (see Supplementary Note 10). However, we find that the NQR frequencies of all Sb sites increase continuously with decreasing temperature with no anomaly across T^* (see Supplementary Fig. 5), indicating that our observation is unlikely due to an orbital order.

The increase of the FWHM of the spectra for all Sb sites below T^* , as can be seen in Fig. 3(b), suggests that the change is an effect related to local charge density. We first consider a charge inhomogeneity as a possible cause. An effect due to charge inhomogeneity related to the sample quality would exist already at high temperatures. Given that the line splitting can only be seen at low temperatures, our observation rather implies an emergence of a possible new charge modulation on top of the star-of-David pattern CDW order. The Sb-NQR line width is much broader than the ^{51}V -NMR linewidth, so only a line broadening is observed down to 5 K. Around T^* , the temperature evolution of

the NMR and NQR spectra is hardly seen. Therefore, we can not confirm whether the additional charge modulation is due to a phase transition or a cross-over. To further investigate this issue, thermodynamic measurements are needed. Note that the amplitude of this modulation is tiny, which can explain why such additional charge modulation was not observed in some STM and X-ray scattering measurements^{22,23}.

Several charge modulation patterns that can be compatible with our NMR data, such as the $4a_0$ ^{24,28}, $4c_0$ ³⁰, and checkboard patterns as shown, in Fig. 4. In this work, we can not distinguish which is the correct pattern. However, we note that the breaking of the in-plane rotational symmetry was observed by measuring c -axis resistivity with the in-plane rotation of the magnetic field⁵². This suggests that the $4a_0$ pattern, which breaks the rotational symmetry, is more likely. The $4a_0$ pattern was also reported by STM measurements^{24,28}. As STM can only obtain the images of surfaces, this $4a_0$ pattern was suggested to be due to electron correlations related to the surface instability and electron-phonon interaction²⁹. In contrast, NMR detects bulk information, so our results suggest a possible $4a_0$ pattern in bulk, forming the nematic order⁵³. Especially, we have noticed that the in-plane anisotropy of the magnetoresistance was observed in the superconducting state, suggesting the twofold feature of superconductivity^{52,54}. Therefore, intertwining between nematicity and superconductivity should be considered for further investigation of the pairing mechanism in CsV_3Sb_5 .

In summary, we have performed NMR and NQR measurements on the kagome superconductor, CsV_3Sb_5 . Below the CDW transition temperature $T_{\text{CDW}} = 98$ K, the abrupt changes of both ^{51}V -NMR and $^{121/123}\text{Sb}$ -NQR spectra indicate that the CDW transition is of the first order. By analyzing the spectra in the CDW state, we suggest that the structural distortion is of the star-of-David type, contrasting with DFT calculations. This implies that electron correlations should be considered for modeling this system. Below $T^* \sim 40$ K, we further find an additional splitting of ^{51}V -NMR lines and broadening of ^{121}Sb -NQR lines, implying the appearance of an additional charge modulation on top of the star-of-David type CDW. All these show that the CDW order in CsV_3Sb_5 is unique, which will be important in future exploration of the relationship between CDW and superconductivity.

Note Added: During the preparation of this manuscript, we became aware of two similar NMR works on CsV_3Sb_5 ^{44,55}. Our ^{51}V -NMR and $^{121/123}\text{Sb}$ -NQR spectra are in good agreement with these two works^{44,55}. The observation of commensurate CDW order and the first-order CDW transition are consistent with their results. However, knowledge about the charge modulation of the CDW order was not reported previously.

METHODS

Samples

Single crystal CsV_3Sb_5 was synthesized by the self-flux method¹⁰. The typical size of the single crystal is around $3 \text{ mm} \times 2 \text{ mm} \times 0.1 \text{ mm}$. T_c was determined by DC susceptibility measured by a superconducting quantum interference device with the applied field 1 Oe parallel to the c -axis (see Supplementary Fig. 1). T_c is close to 3.5 K, which is among the highest values for this compound, indicating its high quality.

NMR and NQR measurements

^{51}V -NMR experiments were performed on one single crystal sample at a fixed magnetic field along the c -axis. The spectra were obtained by adding Fourier transforms of the spin-echo signal recorded for regularly spaced frequency values. $^{121/123}\text{Sb}$ -NQR spectra were measured on a collection of ~ 50 single crystals by sweeping the frequency point by point and integrating spin-echo intensity. By performing EFG calculation, we find that the EFG principal axis of $^{121/123}\text{Sb}$ is along the c -axis (details about EFG calculation is present in Supplementary Note 7). Thus, we arrange the

CsV₃Sb₅ single-crystal flakes along the *c* direction, ensuring the radio-frequency field H_1 in the *ab* plane (see Supplementary Fig. 8).

DATA AVAILABILITY

The data that support the findings of this study are available from the corresponding authors upon reasonable request.

Received: 23 August 2021; Accepted: 16 February 2022;

Published online: 18 March 2022

REFERENCES

- Castro Neto, A. H. et al. The electronic properties of graphene. *Rev. Mod. Phys.* **81**, 109 (2009).
- Yin, J. X. et al. Giant and anisotropic many-body spin-orbit tunability in a strongly correlated kagome magnet. *Nature* **562**, 91–95 (2018).
- Liu, E. K. et al. Giant anomalous hall effect in a ferromagnetic kagome-lattice semimetal. *Nat. Phys.* **14**, 1125–1131 (2018).
- Julien, M.-H. et al. Inhomogeneous magnetism in the doped kagome lattice of LaCuO_{2.66}. *Phys. Rev. B* **87**, 214423 (2013).
- Broholm, C. et al. Quantum spin liquids. *Science* **367**, eaay0668 (2020).
- Fu, M. X., Imai, T., Han, T.-H. & Lee, Y. S. Evidence for a gapped spin-liquid ground state in a kagome Heisenberg antiferromagnet. *Science* **350**, 655–658 (2015).
- Feng, Z. L. et al. Gapped spin-1/2 spinon excitations in a new kagome quantum spin liquid compound Cu₃Zn(OH)₆FBr. *Chin. Phys. Lett.* **34**, 077502 (2017).
- Yan, S. M., Huse, D. A. & White, S. R. Spin-liquid ground state of the $S = 1/2$ kagome Heisenberg antiferromagnet. *Science* **332**, 1173–1176 (2011).
- Zheng, J. C. et al. Gapless spin excitations in the field-induced quantum spin liquid phase of α -RuCl₃. *Phys. Rev. Lett.* **119**, 227208 (2017).
- Ortiz, B. R. et al. New kagome prototype materials: discovery of KV₃Sb₅, RbV₃Sb₅, and CsV₃Sb₅. *Phys. Rev. Mater.* **3**, 094407 (2019).
- Fu, Y. et al. Quantum transport evidence of topological band structures of kagome superconductor CsV₃Sb₅. *Phys. Rev. Lett.* **127**, 207002 (2021).
- Ortiz, B. R. et al. CsV₃Sb₅: A Z₂ topological kagome metal with a superconducting ground state. *Phys. Rev. Lett.* **125**, 247002 (2020).
- Yin, Q. W. et al. Superconductivity and normal-state properties of kagome metal RbV₃Sb₅ single crystals. *Chin. Phys. Lett.* **38**, 037403 (2021).
- Jiang, Y. X. et al. Unconventional chiral charge order in kagome superconductor KV₃Sb₅. *Nat. Mater.* **20**, 1353–1357 (2021).
- Wang, Z. G. et al. Distinctive momentum dependent charge-density-wave gap observed in CsV₃Sb₅ superconductor with topological kagome lattice. Preprint at <https://arxiv.org/abs/2104.05556> (2021).
- Nakayama, K. et al. Multiple energy scales and anisotropic energy gap in the charge-density-wave phase of the kagome superconductor CsV₃Sb₅. *Phys. Rev. B* **104**, L161112 (2021).
- Zhou, X. X. et al. Origin of charge density wave in the kagome metal CsV₃Sb₅ as revealed by optical spectroscopy. *Phys. Rev. B* **104**, L041101 (2021).
- Uykur, E., Ortiz, B. R., Wilson, S. D., Dressel, M. & Tsirlin, A. A. Optical detection of the density-wave instability in the kagome metal KV₃Sb₅. *npj Quantum Mater.* **7**, 16 (2022).
- Ratcliff, N., Hallett, L., Ortiz, B. R., Wilson, S. D. & Harter, J. W. Coherent phonon spectroscopy and interlayer modulation of charge density wave order in the kagome metal CsV₃Sb₅. *Phys. Rev. Mater.* **5**, L111801 (2021).
- Wang, Z. X. et al. Unconventional charge density wave and photoinduced lattice symmetry change in the kagome metal CsV₃Sb₅ probed by time-resolved spectroscopy. *Phys. Rev. B* **104**, 165110 (2021).
- Liu, Z. H. et al. Charge-Density-Wave-Induced bands renormalization and energy gaps in a kagome superconductor RbV₃Sb₅. *Phys. Rev. X* **11**, 041010 (2021).
- Liang, Z. W. et al. Three-dimensional charge density wave and surface-dependent vortex-core states in a kagome superconductor CsV₃Sb₅. *Phys. Rev. X* **11**, 031026 (2021).
- Li, H. X. et al. Observation of unconventional charge density wave without acoustic phonon anomaly in kagome superconductors AV₃Sb₅ (A = Rb, Cs). *Phys. Rev. X* **11**, 031050 (2021).
- Chen, H. et al. Roton pair density wave in a strong-coupling kagome superconductor. *Nature* **599**, 222–228 (2021).
- Shumiya, N. et al. Intrinsic nature of chiral charge order in the kagome superconductor RbV₃Sb₅. *Phys. Rev. B* **104**, 035131 (2021).
- Wang, Z. W. et al. Electronic nature of chiral charge order in the kagome superconductor CsV₃Sb₅. *Phys. Rev. B* **104**, 075148 (2021).
- Wilson, J. A., Di Salvo, F. J. & Mahajan, S. Charge density waves and superlattices in the metallic layered transition metal dichalcogenides. *Adv. Phys.* **24**, 117–201 (1975).
- Zhao, H. et al. Cascade of correlated electron states in the kagome superconductor CsV₃Sb₅. *Nature* **599**, 216–221 (2021).
- Tan, H. X., Liu, Y. Z., Wang, Z. Q. & Yan, B. H. Charge density waves and electronic properties of superconducting kagome metals. *Phys. Rev. Lett.* **127**, 046401 (2021).
- Ortiz, B. R. et al. Fermi surface mapping and the nature of charge density wave order in the kagome superconductor CsV₃Sb₅. *Phys. Rev. X* **11**, 041030 (2021).
- Chen, K. Y. et al. Double superconducting dome and triple enhancement of T_c in the kagome superconductor CsV₃Sb₅ under high pressure. *Phys. Rev. Lett.* **126**, 247001 (2021).
- Yu, F. H. et al. Unusual competition of superconductivity and charge-density-wave state in a compressed topological kagome metal. *Nat. Commun.* **12**, 3645 (2021).
- Zhang, Z. Y. et al. Pressure-induced reemergence of superconductivity in the topological kagome metal CsV₃Sb₅. *Phys. Rev. B* **103**, 224513 (2021).
- Chen, X. et al. Highly robust reentrant superconductivity in CsV₃Sb₅ under Pressure. *Chin. Phys. Lett.* **38**, 057402 (2021).
- Keimer, B., Kivelson, S. A., Norman, M. R., Uchida, S. & Zaanen, J. From quantum matter to high-temperature superconductivity in copper oxides. *Nature* **518**, 179–186 (2015).
- Chen, X. H., Dai, P. C., Feng, D. L., Xiang, T. & Zhang, F.-C. Iron-based high transition temperature superconductors. *Natl. Sci. Rev.* **1**, 371–395 (2014).
- Abragam, A. *The Principles of Nuclear Magnetism* (Oxford Univ. Press, Oxford, 1961).
- Wu, T. et al. Magnetic-field-induced charge-stripe order in the high temperature superconductor YBa₂Cu₃O_y. *Nature* **477**, 191–194 (2011).
- Kawasaki, S. et al. Charge-density-wave order takes over antiferromagnetism in Bi₂Sr_{2-x}La_xCuO₆ superconductors. *Nat. Commun.* **8**, 1267 (2017).
- Blinic, R. & Apih, T. NMR in multidimensionally modulated incommensurate and CDW systems. *Progress in Nuclear Magnetic Resonance Spectroscopy* **41**, 49–82 (2002).
- Vinograd, I. Locally commensurate charge-density wave with three-unit-cell periodicity in YBa₂Cu₃O_y. *Nat. Commun.* **12**, 3274 (2021).
- Ning, F. L. et al. Contrasting spin dynamics between underdoped and overdoped Ba(Fe_{1-x}Co_x)₂As₂. *Phys. Rev. Lett.* **104**, 037001 (2010).
- Zhou, R. et al. Quantum criticality in electron-doped BaFe_{2-x}Ni_xAs₂. *Nat. Commun.* **4**, 2265 (2013).
- Song, D. W. et al. Orbital ordering and fluctuations in a kagome superconductor CsV₃Sb₅. *Science China Physics, Mechanics & Astronomy* **65**, 247462 (2022).
- Zheng, G.-q., Kitaoka, Y., Ishida, K. & Asayama, K. Local hole distribution in the CuO₂ plane of high- T_c Cu-oxides studied by Cu and oxygen NQR/NMR. *J. Phys. Soc. Jpn.* **64**, 2524–2532 (1995).
- Shimajima, T. et al. Orbital-dependent modifications of electronic structure across the magnetostructural transition in BaFe₂As₂. *Phys. Rev. Lett.* **104**, 057002 (2010).
- Zhou, R., Xing, L. Y., Wang, X. C., Jin, C. Q. & Zheng, G.-q. Orbital order and spin nematicity in the tetragonal phase of the electron-doped iron pnictides NaFe_{1-x}Co_xAs. *Phys. Rev. B* **93**, 060502(R) (2016).
- Lin, Y. P. & Nandkishore, R. M. Complex charge density waves at Van Hove singularity on hexagonal lattices: Haldane-model phase diagram and potential realization in the kagome metals AV₃Sb₅ (A = K, Rb, Cs). *Phys. Rev. B* **104**, 045122 (2021).
- Baek, S.-H. et al. Orbital-driven nematicity in FeSe. *Nat. Mater.* **14**, 210–214 (2015).
- Zhou, R. et al. Singular magnetic anisotropy in the nematic phase of FeSe. *npj Quantum Mater.* **5**, 93 (2020).
- Yang, J. et al. New superconductivity dome in LaFeAsO_{1-x}F_x accompanied by structural transition. *Chin. Phys. Lett.* **32**, 107401 (2015).
- Xiang, Y. et al. Twofold symmetry of *c*-axis resistivity in topological kagome superconductor CsV₃Sb₅ with in-plane rotating magnetic field. *Nat. Commun.* **12**, 6727 (2021).
- Christensen, M. H., Birol, T., Andersen, B. M. & Fernandes, R. M. Theory of the charge-density wave in AV₃Sb₅ kagome metals. *Phys. Rev. B* **104**, 214513 (2021).
- Ni, S. L. et al. Anisotropic superconducting properties of kagome metal CsV₃Sb₅. *Chin. Phys. Lett.* **38**, 057403 (2021).
- Mu, C. et al. S-wave superconductivity in kagome metal CsV₃Sb₅ revealed by ¹²¹/₁₂₃Sb NQR and ⁵¹V NMR measurements. *Chin. Phys. Lett.* **38**, 077402 (2021).

ACKNOWLEDGEMENTS

The authors thank Kun Jiang and Hui Chen for valuable discussions. This work was supported by the National Natural Science Foundation of China (Grant Nos. 11974405, Nos. 61888102, Nos. 51771224 and Nos. 11904023), the National Key Research and Development Projects of China (Grant Nos. 2017YFA0302904, Nos. 2018YFA0305800).

and 2019YFA0308500) and the Strategic Priority Research Program of the Chinese Academy of Sciences (Grant Nos. XDB33010100 and Nos. XDB33030100). This work was supported by the Synergic Extreme Condition User Facility.

AUTHOR CONTRIBUTIONS

The single crystals were grown by Z.Z., H.T.Y. and H.J.G. The NMR measurements were performed by J.L., Z.Y.Z., J.Y., A.F.F. and R.Z. R.Z. and G.-q.Z. wrote the manuscript with inputs from J.L. All authors have discussed the results and the interpretation.

COMPETING INTERESTS

The authors declare no competing interests.

ADDITIONAL INFORMATION

Supplementary information The online version contains supplementary material available at <https://doi.org/10.1038/s41535-022-00437-7>.

Correspondence and requests for materials should be addressed to J. Luo, H. T. Yang or R. Zhou.

Reprints and permission information is available at <http://www.nature.com/reprints>

Publisher's note Springer Nature remains neutral with regard to jurisdictional claims in published maps and institutional affiliations.



Open Access This article is licensed under a Creative Commons Attribution 4.0 International License, which permits use, sharing, adaptation, distribution and reproduction in any medium or format, as long as you give appropriate credit to the original author(s) and the source, provide a link to the Creative Commons license, and indicate if changes were made. The images or other third party material in this article are included in the article's Creative Commons license, unless indicated otherwise in a credit line to the material. If material is not included in the article's Creative Commons license and your intended use is not permitted by statutory regulation or exceeds the permitted use, you will need to obtain permission directly from the copyright holder. To view a copy of this license, visit <http://creativecommons.org/licenses/by/4.0/>.

© The Author(s) 2022